

Article

Synthesis, Structure, and Photomagnetic Properties of a Hydrogen-Bonded Lattice of $[\text{Fe}(\text{bpp})_2]^{2+}$ Spin-Crossover Complexes and Nicotinate Anions

Verónica Jornet-Mollá , Carlos Giménez-Saiz and Francisco M. Romero * 

Instituto de Ciencia Molecular, Universitat de València, P.O. Box 22085, 46071-Valencia, Spain; Veronica.Jornet@uv.es (V.J.-M.); Carlos.Gimenez@uv.es (C.G.-S.)

* Correspondence: fmmr@uv.es; Tel.: +34-963-54-44-05; Fax: +34-963-54-32-73

Received: 3 November 2018; Accepted: 19 November 2018; Published: 21 November 2018



Abstract: In this paper, we report on the synthesis, crystal structure, and photomagnetic properties of the spin-crossover salt of formula $[\text{Fe}(\text{bpp})_2](\text{C}_6\text{H}_4\text{NO}_2)_2 \cdot 4\text{H}_2\text{O}$ ($1 \cdot 4\text{H}_2\text{O}$) (bpp = 2,6-bis(pyrazol-3-yl)pyridine; $\text{C}_6\text{H}_4\text{NO}_2^-$ = nicotinate anion). This compound exhibits a 3D supramolecular architecture built from hydrogen bonds between iron(II) complexes, nicotinate anions, and water molecules. As synthesized, the hydrated material is low-spin and desolvation triggers a low-spin (LS) to high-spin (HS) transformation. Anhydrous phase **1** undergoes a partial spin crossover ($T_{1/2} = 281$ K) and a LS to HS photomagnetic conversion with a $T(\text{LIESST})$ value of 56 K.

Keywords: spin-crossover; LIESST effect; hydrogen bonding; π - π interactions

1. Introduction

Switching magnetic materials represent a prominent avenue for the construction of multifunctional materials with several applications in different fields, such as chemical and pressure sensing [1], data storage [2], and spintronics [3,4]. The most studied spin-crossover (SCO) centres are based on iron(II) complexes that exhibit labile electronic configurations switchable between $^1\text{A}_1$ low-spin (LS; $S = 0$) and $^5\text{T}_2$ high-spin (HS; $S = 2$) states as a consequence of a given external perturbation, such as light irradiation, variation of temperature and/or pressure [5–11]. The response to these external stimuli leads to different changes in magnetism, colour, and structure. In particular, important variations of the Fe–N metal–ligand bond lengths (0.1–0.2 Å) and N–Fe–N angles (0.5–8°) are observed upon spin crossover [12]. Depending on the cooperativity of the system, the spin transition may be abrupt with hysteretic behaviour (memory effect) and with drastic changes in optical and magnetic properties. The appearance of hysteresis and thus cooperativity in a solid system can be achieved when the geometrical distortion is propagated to the whole framework, providing the material with a bistable character.

Therefore, under the same conditions, a bistable system can be localized either in the LS or in the HS state and the possibility of finding a specific state depends on the history of the material. This is a desirable situation for the development of technological applications such as quantum logic operators or components in memory storage devices, mainly when the effects proceed at room temperature [13–17]. In order to achieve high levels of cooperativity, various synthetic strategies have been developed [18]. One way consists in the use of rigid bridging ligands as connectors between the Fe^{2+} cations; this strategy has yielded a wide range of 1-3D SCO coordination polymers [19–22]. Another type of communication between the coordination centres is provided by hydrogen bonding,

which is likely to be responsible for the dependence of magnetic properties on the extent of solvation observed in many compounds [23,24].

In this context, the family of bis-chelated iron(II) complexes with the formula $[\text{Fe}(\text{bpp})_2]\text{X}_2$ (bpp being the tridentate ligand 2,6-bis(pyrazol-3-yl)pyridine, Chart 1) is very interesting. In these spin-crossover salts with pseudo C_{2v} symmetry, the imine N atom coordinates to the Fe^{2+} cation and the non-coordinating NH groups allow for interaction through hydrogen bonding between the bpp ligands and anions or solvate molecules present in the lattice. The paramount role of the hydrogen bonds on the SCO features is largely documented in molecular compounds [25,26] and has been extensively studied in these salts [27].

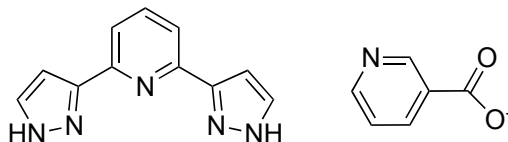


Chart 1. Structures of bpp and nicotinate anion.

In addition, these compounds are attractive due to the fact that the desolvated material usually exhibits very abrupt transitions and presents light-induced excited spin-state trapping (LIESST) effects [28], with long-lived lifetimes of the photoinduced metastable phases [29–31].

In a recent report, we introduced a rational design of SCO materials exhibiting ferroelectricity [32]. This is based on the use of hydrogen bonds in the assembly of the $[\text{Fe}(\text{bpp})_2]^{2+}$ complexes with isonicotinate anions. From the point of view of the connectivity of the lattice, the iron(II) complex acts as a 4-fold pseudotetrahedral H-bond donor, whereas the isonicotinate anion acts as a non-centrosymmetric H-bond acceptor. This necessarily yields a non-centrosymmetric diamondoid lattice. In the present work, the isonicotinate anion has been replaced with the nicotinate anion (nic = 3-pyridinecarboxylate, Chart 1) in order to study the effect of the position of the nitrogen atom on the properties of the resulting material. Herein, we report on the synthesis, crystal structure, and photomagnetic properties of the title compound, $[\text{Fe}(\text{bpp})_2](\text{nic})_2 \cdot 4\text{H}_2\text{O}$ ($1 \cdot 4\text{H}_2\text{O}$).

2. Materials and Methods

2.1. Physical Measurements

Magnetic susceptibility measurements were performed on polycrystalline samples using a magnetometer (Quantum Design MPMS-XL-5, San Diego, CA, USA) equipped with a SQUID (Superconducting Quantum Interference Device) sensor. Variable temperature measurements were carried out in the temperature range 2–400 K in a magnetic field of 0.1 T. The temperature sweeping rates were as follows: $1 \text{ K} \cdot \text{min}^{-1}$ (2–20 K), $2.25 \text{ K} \cdot \text{min}^{-1}$ (20–200 K), and $1.25 \text{ K} \cdot \text{min}^{-1}$ (200–400 K). A dehydrated sample of **1** was obtained *in situ* by maintaining the sample in the SQUID at 400 K for 1 h (until a constant magnetic signal was obtained) and on plastic capsules perforated in order to favour solvent loss. For photomagnetic measurements, the sample was prepared in a thin layer to promote full light penetration. First, the sample was dehydrated *in situ* in the SQUID device at 400 K for 1 h. After slow cooling to 10 K, the sample was irradiated with green light ($\lambda = 532.06 \text{ nm}$) and the magnetization was measured. When the saturation point was reached, the laser was switched off and the temperature increased at a rate of $0.3 \text{ K} \cdot \text{min}^{-1}$ to determine the $T(\text{LIESST})$ value given by the minimum of the $\delta(\chi T)/\delta T$ versus T curve for the relaxation process.

Thermogravimetric (TG) measurements of $\text{Ag}(\text{C}_6\text{H}_4\text{NO}_2)$ were carried out under O_2 atmosphere in a Setsys TGA-ATD16/8 apparatus (Setaram Instrumentation, Caluire, France) the 298–1000 K temperature range at a scan rate of $10 \text{ K} \cdot \text{min}^{-1}$. TG analysis of $1 \cdot 4\text{H}_2\text{O}$ was performed in a TGA/SDTA/851e apparatus (Mettler Toledo, Columbus, OH, USA) under N_2 atmosphere in the 298–973 K range at a scan rate of $10 \text{ K} \cdot \text{min}^{-1}$.

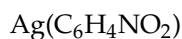
Differential scanning calorimetry (DSC) measurements under nitrogen atmosphere were performed in a DSC 821e apparatus (Mettler Toledo, OH, USA) with warming and cooling rates equal to $10 \text{ K} \cdot \text{min}^{-1}$. A correction from the sample holder was automatically applied.

Infrared (IR) transmission measurements of potassium bromide pellets were recorded at room temperature with a Nicolet Avatar 320 FT-IR spectrophotometer (Thermo Electron, Waltham, MA, USA) in the range $4000\text{--}400 \text{ cm}^{-1}$. CHN elemental analyses were carried out in a EA 1110 CHNS analyser (CE Instruments, Wigan, United Kingdom).

Powder X-ray diffraction measurements were collected using Cu $K\alpha$ radiation ($\lambda = 1.54056 \text{ \AA}$) at room temperature in a 2θ range from 2 to 40° . A polycrystalline sample of $1 \cdot 4\text{H}_2\text{O}$ was lightly ground in an agate mortar and filled into a 0.5 mm borosilicate capillary prior to being mounted and aligned on an Empyrean powder diffractometer (Pananalytical, Cambridge, United Kingdom). The simulated diffractogram was obtained from single crystal X-ray data using the CrystalDiffract software (CrystalMaker Software Ltd., Begbroke, United Kingdom).

2.2. Synthesis

Ligand bpp was prepared using the previously published procedure [33]. All other reagents and solvents were purchased from commercial sources, with no further purification being undertaken.



A suspension of nicotinic acid (1.230 g , 10 mmol) in 25 ml of a mixture $3:2 \text{ EtOH}/\text{H}_2\text{O}$ was treated with a suspension of silver carbonate (1.371 g , 5 mmol) in $25 \text{ ml H}_2\text{O}$. Then, the mixture was refluxed for 3 h and 30 min until CO_2 ceased to evolve. There was a change in the colour of the solid from yellow-brown to white. The product was collected using filtration and washed with water and acetone to yield 1.988 g (87%) of the desired compound. We found: C, 30.58 ; H, 1.80 ; N, 6.01 . $\text{C}_6\text{H}_4\text{AgNO}_2$ requires C, 31.33 ; H, 1.75 ; N, 6.09 (the sample contained some humidity, equivalent to $0.25 \text{ H}_2\text{O}$ molecules per formula). Thermogravimetric analysis (Figure S1) confirmed the anhydrous character of this salt. $\nu_{\text{max}}/\text{cm}^{-1}$: 3400.4 , 3042.9 , 1593.9 , 1549.3 , 1387.4 , 1196.0 , 1088.4 , 1022.2 , 840.4 , 758.4 , 704.3 , 511.2 .



$\text{FeCl}_2 \cdot 4\text{H}_2\text{O}$ (0.0994 g , 0.5 mmol) was added as a solid to a degassed solution of bpp (0.212 g , 1.0 mmol) in 20 ml of a mixture $4:1 \text{ MeOH}/\text{H}_2\text{O}$. A deep red colour appeared. After complete dissolution of the iron reagent, a mixture of $\text{Ag}(\text{C}_6\text{H}_4\text{NO}_2)$ (230 mg , 1 mmol) in $20 \text{ ml H}_2\text{O}$ was added. After stirring for 1 h at 65°C , the yellowish precipitate of AgCl was filtered through a low-porosity frit. The filtrate was left undisturbed. Red prisms suitable for X-ray analysis appeared after a few days, yielding 246.3 mg (62%). We found: C, 51.63 ; H, 4.13 ; N, 21.83 . $\text{C}_{34}\text{H}_{34}\text{FeN}_{12}\text{O}_8$ requires C, 51.40 ; H, 4.31 ; N, 21.15 (the sample was partially dehydrated, losing $0.55 \text{ H}_2\text{O}$ molecules per formula prior to analysis). $\nu_{\text{max}}/\text{cm}^{-1}$: 3422.8 , 1601.0 , 1560.3 , 1438.4 , 1385.0 , 1281.1 , 1234.5 , 1146.1 , 1094.1 , 1028.3 , 897.0 , 831.3 , 756.8 , 697.9 , 619.8 .

2.3. X-ray Crystallography

A suitable crystal of $1 \cdot 4\text{H}_2\text{O}$ was coated with Paratone N oil, suspended on a small fiber loop, and placed in a stream of cold nitrogen (120 K) on an Oxford Diffraction Supernova diffractometer equipped with a graphite-monochromated Enhance Mo X-Ray Source ($\lambda = 0.71073 \text{ \AA}$). The data collection routines, unit cell refinements, and data processing were carried out using the CrysAlisPro v38.46 software package (Rigaku, The Woodlands, TX, USA). The structure was solved using the SHELX package [34]. The asymmetric unit of $1 \cdot 4\text{H}_2\text{O}$ contains one $[\text{Fe}(\text{bpp})_2]^{2+}$ cation, two nicotinate anions, and four water molecules, all in general positions. H atoms bonded to carbon atoms were included at calculated positions and refined with a rigid model. H atoms of bpp amino groups were all found in Fourier difference maps and refined positionally with the geometrical restraint $\text{N-H} = 0.89 \text{ \AA}$.

Moreover, all H atoms on water molecules were found in difference maps and refined using geometrical restraints (O–H = 0.82 Å and H···H = 1.30 Å). The chemical formula of this compound includes the total number of hydrogen atoms and all non-hydrogen atoms were refined anisotropically. CCDC1832023 contain the supplementary crystallographic data for 1·4H₂O at 120 K. These data were provided free of charge by the Cambridge Crystallographic Data Centre.

3. Results

3.1. Synthesis and Thermal Properties

In order to avoid the inclusion of undesired counterions in the spin-crossover network, it is necessary to obtain a solution without any other hydrogen-bond acceptors that could be in competition with the nicotinate anions. To achieve this goal, it has been shown that the use of a metathesis reaction gives excellent results [32,35–37]. Based on this, we performed a metathesis reaction of silver nicotinate with [Fe(bpp)₂]Cl₂ that resulted in the precipitation of AgCl, yielding a solution free from the undesired chloride anions.

TG analysis of 1·4H₂O under nitrogen atmosphere (Figure S2) was performed in order to determine at which temperature the dehydration of the sample starts and the temperature range of the stability of the compound. This will determine the most suitable thermal conditions for magnetism experiments. The first loss of water molecules takes place at 327 K with a weight decrease of 6.3 %, which is related to the loss of about three water molecules per iron cation. The fourth water molecule comes off at temperatures near the thermal decomposition of the sample (2.2%, in the 443–493 K temperature range). These results show a good agreement with the formulation determined from the X-ray crystal structure experiment and elemental analysis. The fact that the loss of water molecules takes place in two separate steps indicates the existence of different types of water molecules in the crystal structure.

The DSC measurement (Figure S3) is in accordance with the thermogravimetric data. The as synthesized material does not show any feature upon cooling down to 133 K (black line). In the first heating process (curve 1), there is a very intense endothermic peak around 334 K that fits in the temperature range where the loss of three water molecules is observed. Therefore, this endothermic peak has been associated with the dehydration of the sample. The subsequent cooling plot (curve 2) shows a broad feature between 373 and 323 K and three very weak exothermic peaks at 282, 262, and 218 K. The intensities ascribed to these peaks are very low, meaning that this might be either a result of a partial spin-crossover process and/or evidence of a phase transition. The second heating process (curve 3) presents three endothermic peaks centred at 229, 264, and 289 K, indicating that these processes are reversible and proceed with thermal hysteresis. Values of enthalpy and entropy changes associated with them are gathered in Table S1. Summing up the contributions of the three peaks gives a total enthalpy change $\Delta H = 4.8 \text{ kJ}\cdot\text{mol}^{-1}$ and entropy change $\Delta S = 20.6 \text{ J}\cdot\text{K}^{-1}\cdot\text{mol}^{-1}$ (average values obtained from the cooling and warming curves). These parameters are weak but lie within the range expected for spin crossover.

3.2. Structural Description

1·4H₂O crystallizes in the non-centrosymmetric and polar *Pc* monoclinic space group (Table 1). The crystal structure contains only one crystallographically independent (Figure 1) Fe(II) centre, Fe1, and two inequivalent anions in the structure. The independent Fe²⁺ site is located in a general position and is bound to two bpp tridentate ligands in mutual perpendicular orientations. Therefore, the iron(II) coordination environment is the well-known octahedral FeN₆ with the highest possible *D*_{2d} local symmetry of the [Fe(bpp)₂]²⁺ cations. The Fe–N(pyridine) bond distances (mean value $\approx 1.9264(25)$) are slightly shorter than those corresponding to the Fe–N(pyrazole) bonds (mean value $\approx 1.964(8)$). In any case, the Fe–N bond distances are lower than 2.0 Å, thus revealing a low-spin ground state for the Fe²⁺ cation, which is the expected stable spin state observed in similar hydrated compounds [37–39].

With respect to the second iron coordination sphere, each $[\text{Fe}(\text{bpp})_2]^{2+}$ complex is hydrogen-bonded to only two nicotinate anions and two water molecules. The N atoms of the isonicotinate anion do not establish interactions with the bpp ligand and are hydrogen-bonded to crystallization water molecules present in the network.

Table 1. Summary of crystal data.

Compound	1·4H ₂ O
Formula	C ₃₄ H ₃₄ FeN ₁₂ O ₈
Formula weight	794.58
Crystal system	Monoclinic
Space group	<i>Pc</i>
<i>a</i> /Å	8.17633(10)
<i>b</i> /Å	8.15854(9)
<i>c</i> /Å	26.9671(3)
α /°	-
β /°	92.0138(10)
γ /°	-
<i>V</i> /Å ³	1797.78(4)
<i>Z</i>	2
<i>T</i> /K	120(2)
ρ_{calcd} /g·cm ⁻³	1.468
λ /Å	0.71073
θ -range/°	2.870–29.963
No. of rflns. collected	84313
No. of indep. rflns./ <i>R</i> _{int}	9867/0.0635
Restraints/parameters	18/532
<i>R</i> ₁ / <i>wR</i> ₂ (<i>I</i> > 2σ(<i>I</i>)) ¹	0.0324/0.0664
<i>R</i> ₁ / <i>wR</i> ₂ (all data) ¹	0.0398/0.0711
$\Delta\rho_{\text{max}}$ and $\Delta\rho_{\text{min}}$ /e·Å ⁻³	0.265/−0.395
Absolute structure parameter	−0.016(5)

$$^1 R_1 = \Sigma(F_o - F_c) / \Sigma(F_o); wR_2 = [\Sigma w(F_o^2 - F_c^2)^2 / \Sigma w(F_o^2)]^{1/2}.$$

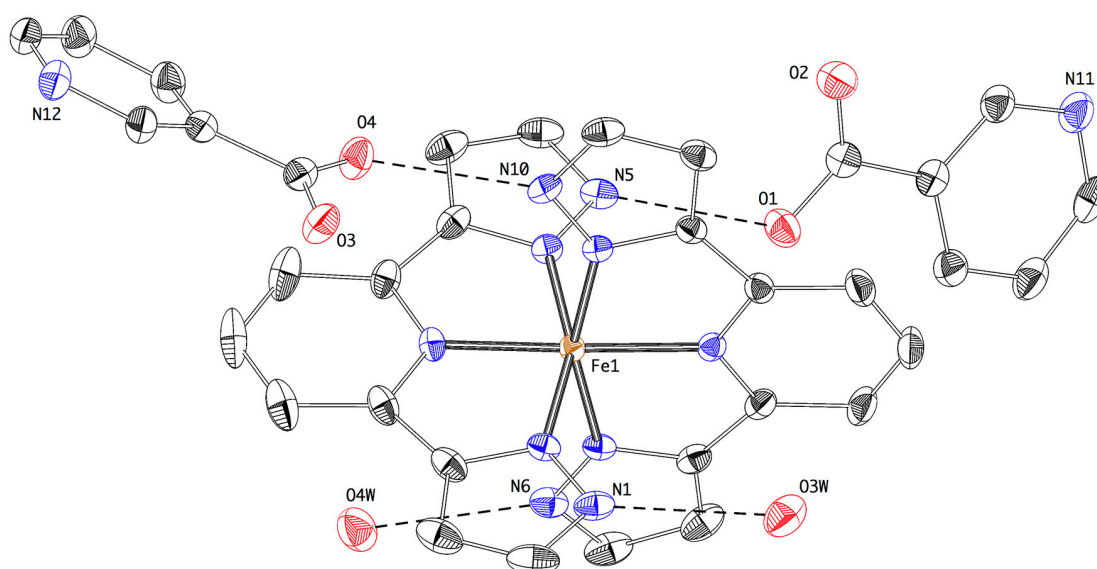


Figure 1. Thermal ellipsoid plot of the crystal structure of 1·4H₂O showing the $[\text{Fe}(\text{bpp})_2]^{2+}$ complex, the two crystallographically independent nicotinate anions, and the two water molecules present in the second coordination sphere of the iron site. Dashed lines refer to H bonds. Thermal ellipsoids are drawn at a 50% probability level. H atoms are not shown.

The crystal structure is best described as a packing of layers of $[\text{Fe}(\text{bpp})_2]^{2+}$ cations and nicotinate anions that alternate along the c axis (Figure 2). These cationic and anionic layers are held together thanks to the existence of hydrogen bonds, either directly or involving water molecules of crystallization.

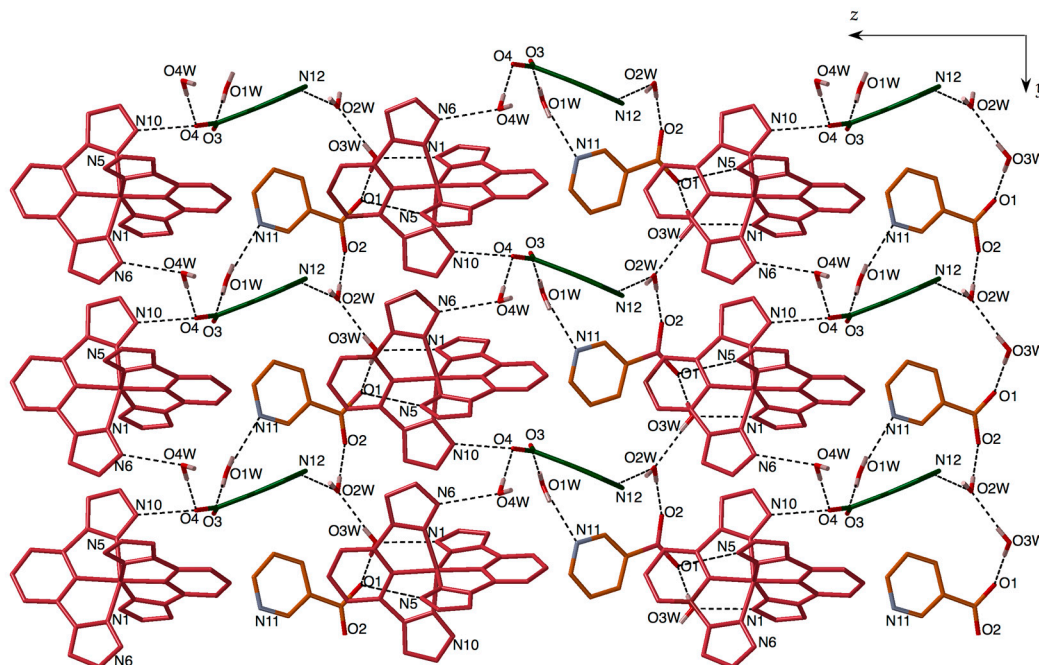


Figure 2. A view of the crystal structure of $1.4\text{H}_2\text{O}$ along the a axis, showing the alternation of $[\text{Fe}(\text{bpp})_2]^{2+}$ cationic layers and nicotinate anionic layers. The iron complexes are illustrated in red whereas the two independent nicotinate anions are depicted in orange and green. The dashed lines refer to hydrogen bonds. Only the H atoms of water molecules are shown.

The nicotinate anions and water molecules occupy the space between the $[\text{Fe}(\text{bpp})_2]^{2+}$ cationic layers. A view parallel to the sheets (Figure 2) shows the two independent nicotinate anions depicted in different colours. The first one (illustrated in orange in Figure 2) is hydrogen-bonded to three water molecules (O1W, O2W and O3W) and one $[\text{Fe}(\text{bpp})_2]^{2+}$ cation (N5). The other nicotinate anion (depicted in green) is also hydrogen-bonded to three water molecules (O1W, O2W and O4W) and one $[\text{Fe}(\text{bpp})_2]^{2+}$ cation (N10). Therefore, the common feature is that they are connected to only one Fe^{2+} centre using one oxygen atom that is simultaneously hydrogen-bonded to one water molecule, the other oxygen atom and the nitrogen of the pyridine unit being engaged in hydrogen bonding with additional water molecules. Both anions alternate in the interlayer space along the y direction. Relevant hydrogen-bonding parameters are gathered in Table S2.

The cationic layers exhibit the typical pseudotetragonal *terpyridine embrace* motif, in which each $[\text{Fe}(\text{bpp})_2]^{2+}$ cation interacts with four neighbouring iron units via π - π stacking interactions (Figure 3). Equivalent bpp ligands form stacks along the a and b axes with the shortest distances between adjacent pyrazolyl mean planes equal to 3.256(3) Å (C11...N1) and 3.284(3) Å (C22...N6), respectively. Across the third direction, the iron complexes of consecutive layers are twisted with respect to each other and shifted along the y direction, resulting in an alternated packing of the type AA'AA'.

A projection of the crystal packing onto the ab plane (Figure 4) shows the presence of two different types of water molecules: the ones that form the layers through direct hydrogen bonds with the bpp ligands (O3W and O4W), and the ones that fill the voids within the layers (O1W and O2W).

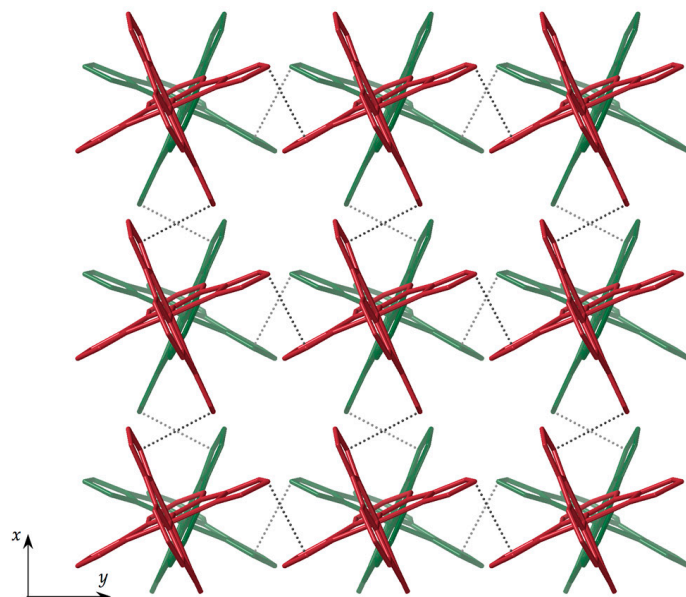


Figure 3. A view of the crystal packing of $1\cdot 4\text{H}_2\text{O}$ parallel to the c axis showing two consecutive $[\text{Fe}(\text{bpp})_2]^{2+}$ cationic layers in different colours (nicotinate anions and water molecules are omitted). The dotted lines refer to π - π stacking interactions. H atoms are not shown.

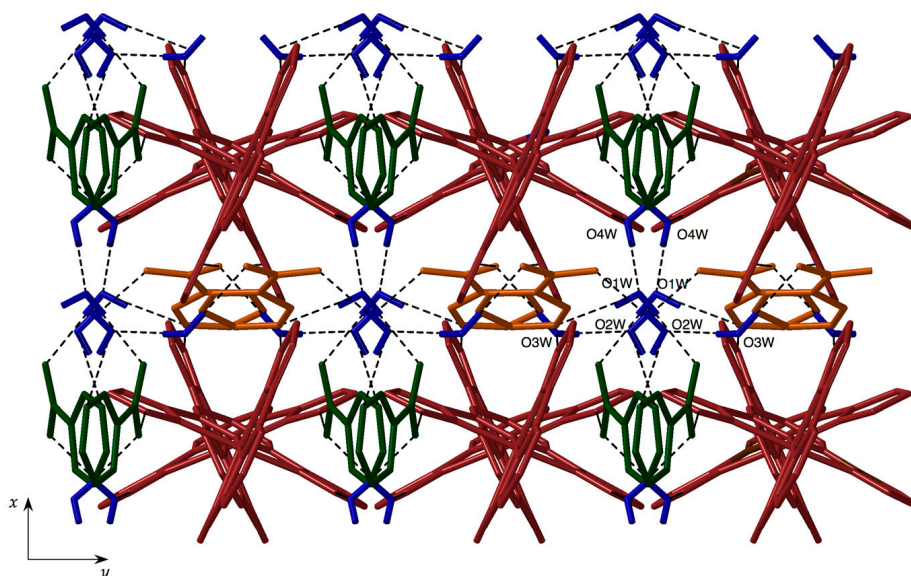


Figure 4. A view of the 2D packing of $1\cdot 4\text{H}_2\text{O}$ along the c axis, showing the two different kinds of water molecules that are represented in blue: those filling the voids (O1W and O2W), and those forming the layers (O3W and O4W). Only the H atoms of water molecules are shown.

Powder X-ray diffraction (PXRD) experiments have been performed and Figure 5 shows the comparison between the X-ray diffractogram measured at room temperature of the bulk sample and the simulated diffractogram from the single crystal data recorded at 120 K. It can be seen that there is a good agreement between both patterns, discarding the presence of impurities and excluding the existence of a phase transition between 120 K and room temperature.

Temperature-dependent PXRD data (Figure S4) show that the sample maintained the same diffraction pattern upon heating from 298 K to 353 K, where at least three H_2O molecules were lost. Instead, heating up to 400 K resulted in amorphization. We attribute this change to complete dehydration (loss of the fourth water molecule). The discrepancy between this behaviour and the thermogravimetric data comes from the fact that TGA is performed at a high-temperature sweeping

rate, whereas PXRD is done in static conditions. We also used PXRD to check the integrity of the sample after dehydration. For that purpose, a sample of $1 \cdot 4\text{H}_2\text{O}$ was placed in a Schlenk tube and heated under vacuum at 400 K for 2 h. Then, the sample was allowed to rehydrate. An identical diffractogram to the one recorded for the original sample was obtained (Figure S5), even after another dehydration-rehydration cycle, confirming both the integrity of the sample and the reversibility of the dehydration process.

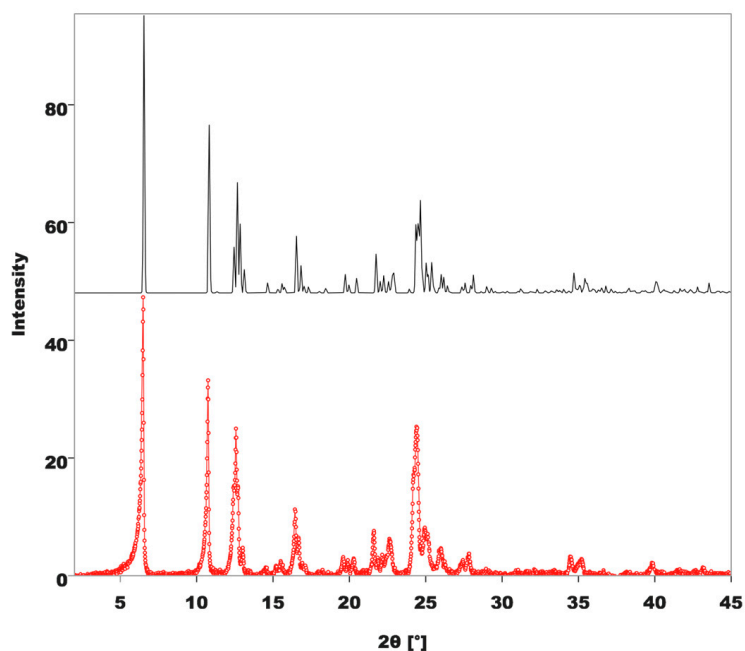


Figure 5. Comparison of the powder diffractogram of $1 \cdot 4\text{H}_2\text{O}$ (in red) with the simulation obtained from single crystal data (in black).

3.3. Magnetic Properties

The temperature dependence of the χT product (χ = molar magnetic susceptibility; T = absolute temperature) is shown in Figure 6. At low temperatures, the sample is diamagnetic, as expected for a low-spin ground state for this Fe(II) complex. Above room temperature, χT increases continuously on heating up to 400 K, where it equals $3.21 \text{ emu} \cdot \text{K} \cdot \text{mol}^{-1}$. This value is the one expected for a high-spin Fe^{2+} cation per formula ($\geq 3.0 \text{ emu} \cdot \text{K} \cdot \text{mol}^{-1}$), indicating a complete spin crossover triggered by the dehydration of the sample. Upon cooling, χT decreases continuously and reaches a critical point at 283 K (corresponding to the first transition seen in DSC, cooling mode), where $\chi T = 2.21 \text{ emu} \cdot \text{K} \cdot \text{mol}^{-1}$ (fraction of high-spin centres $\gamma_{\text{HS}} \approx 2/3$). Then, it decreases more abruptly until $T = 273 \text{ K}$, and then smoothly to reach a plateau below 83 K, where $\chi T = 0.41 \text{ emu} \cdot \text{K} \cdot \text{mol}^{-1}$ (fraction of high-spin centres $\gamma_{\text{HS}} \approx 1/8$). Below 15 K, χT decreases sharply due to zero-field splitting effects.

The second heating curve matches the cooling plot until 245 K, when a hysteresis loop opens ($\Delta T \approx 30 \text{ K}$). The hysteretic behaviour disappears above a critical point located at 307 K, where the cooling and heating curves merge and both reach practically a saturation value corresponding to a 100% HS material. The width of the thermal hysteresis loop is highly dependent on the thermal treatment at 400 K. If this annealing is avoided, a very similar $\chi T = f(T)$ plot is obtained (showing two discontinuities around 280 K and 290 K, and a limiting low-temperature value corresponding to $\gamma_{\text{HS}} \approx 1/8$), but now the hysteresis disappears. It is thus important to ensure the complete dehydration and thermal annealing of the sample to obtain reproducible results.

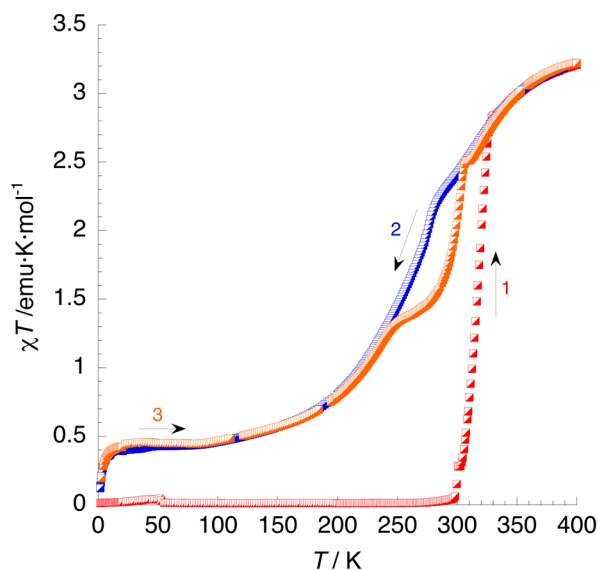


Figure 6. Thermal variation of χT of $1\cdot 4\text{H}_2\text{O}$. Curve 1: first heating process (the bump observed around 50 K is due to the presence of oxygen). Curves 2 and 3: first cooling and second heating processes, respectively.

3.4. Photomagnetic Studies

Figure 7 shows the results of the photomagnetic experiments recorded using a SQUID magnetometer. Before irradiation, the sample was dehydrated in situ in the SQUID device at 400 K for 1 h. Then, at 10 K, the LS sample (initially with almost all the iron centres in their LS states) was irradiated using green laser light ($\lambda = 532.06$ nm, no photomagnetic response was observed under red light). There was an abrupt increase in magnetic susceptibility, which reached saturation at a value of ca. $2 \text{ emu}\cdot\text{K}\cdot\text{mol}^{-1}$, indicating approximately a 2/3 conversion of the iron sites to the metastable HS state. The fraction of iron sites that is reluctant to photoexcitation corresponds to the fraction of HS centres undergoing SCO at high temperatures (higher than room temperature). The light was then turned off and the sample warmed in the dark at a heating rate of $0.3 \text{ K}/\text{min}$, according to the standardised $T(\text{LIESST})$ procedure [28]. The compound remains in its trapped HS state until $T(\text{LIESST}) = 56 \text{ K}$ (calculated as the minimum of the derivative $\delta(\chi T)/\delta T$). At higher temperatures, complete relaxation of the metastable HS content is seen and χT reaches a minimum value of $0.5 \text{ emu}\cdot\text{K}\cdot\text{mol}^{-1}$, close to the residual fraction of HS centres (1/8) measured before irradiation.

A database containing more than sixty iron(II) spin-crossover materials with nitrogen-donor ligands [28,40] made it possible to establish empirical correlations between $T(\text{LIESST})$ and the thermal spin transition temperature, $T_{1/2}$. Based on these data, it has been shown that the following linear expression:

$$T(\text{LIESST}) = T_0 - 0.3T_{1/2} \quad (1)$$

governs the photomagnetic properties of most of these compounds, where T_0 is an empirical parameter that depends mainly on the distortion of the octahedral coordination sphere (for $[\text{Fe}(\text{bpp})_2]^{2+}$ complexes: $T_0 = 150 \text{ K}$) [28].

Considering that $T_{1/2} = 281 \text{ K}$ (the average value between $T_{1/2}^\uparrow$ and $T_{1/2}^\downarrow$), Equation 1 yields $T(\text{LIESST}) = 66 \text{ K}$, which is in rough agreement with the experimental value.

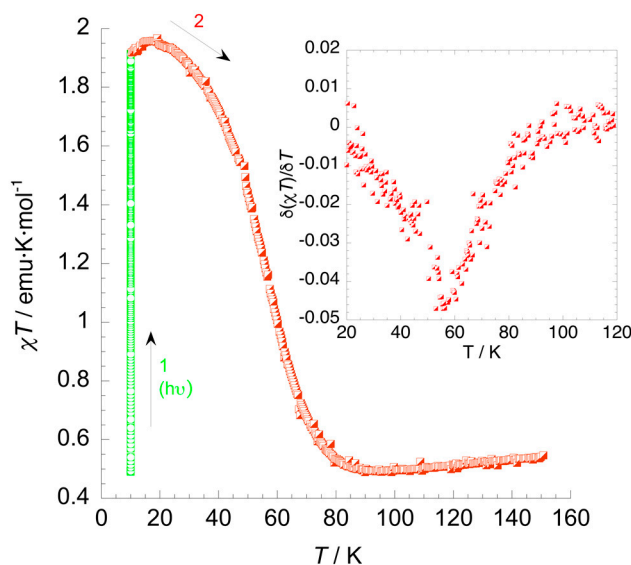


Figure 7. Photomagnetic properties of **1**. Curve 1 (green): Irradiation at 10 K. Curve 2 (orange): Thermal variation of χT upon heating at a scan rate of $0.3 \text{ K}\cdot\text{min}^{-1}$. The inset shows the first derivative plot of the $T(\text{LIESST})$ curve.

4. Conclusions

In this paper, we have described the synthesis, structure, and magnetic properties of a new hydrogen-bonded network that contains $[\text{Fe}(\text{bpp})_2]^{2+}$ cations and nicotinate anions. It is tempting to compare $1\cdot 4\text{H}_2\text{O}$ with the previously reported $[\text{Fe}(\text{bpp})_2](\text{isonic})_2\cdot 2\text{H}_2\text{O}$ [32]. In this compound, thanks to the linearity of the isonicotinate anion, robust hydrogen bonds can be established between the bpp ligands and the isonicotinate anions occupying the four available positions in the second iron coordination sphere. This provides a strong directionality and allows for the prediction of the connectivity of the resulting structure. Nevertheless, in the case of compound $1\cdot 4\text{H}_2\text{O}$, the angular character of the nicotinate anion makes the formation of these interactions more difficult, allowing for the presence of water molecules in the second iron coordination sphere. Another possible reason for the different behaviour of these similar salts could be the slightly different basicities of the nicotinate ($\text{p}K = 4.77$) and isonicotinate ($\text{p}K = 4.90$) anions, the latter being a stronger N-donor [41]. In any case, the final result is that π - π stacking interactions are predominant and the *terpyridine embrace* motif is stabilized.

Differential scanning calorimetry analysis and magnetic characterization of compound $1\cdot 4\text{H}_2\text{O}$ show a conversion from the LS state to the HS state after the loss of water molecules. The anhydrous material obtained exhibits spin crossover with relatively high cooperativity and with an associated hysteretic behaviour. Furthermore, this compound presents an LIESST effect and can be partially switched from the diamagnetic LS state to the paramagnetic HS state using green light at 10 K. The value of $T(\text{LIESST})$ obtained (56 K) is consistent with those previously reported for other iron(II) complexes of bpp ligands [37]. Unfortunately, the compound loses its crystallinity upon dehydration and the lack of a structural characterization of the anhydrous phase precludes the establishment of structure-property correlations.

Supplementary Materials: The following are available online at <http://www.mdpi.com/2073-4352/8/11/439/s1>: Figure S1: Thermogravimetric analysis of $\text{Ag}(\text{C}_6\text{H}_4\text{NO}_2)$; Figure S2: Thermogravimetric analysis of $1\cdot 4\text{H}_2\text{O}$; Figure S3: Differential scanning calorimetry of $1\cdot 4\text{H}_2\text{O}$; Figures S4-S5: Powder X-ray diffractograms of $1\cdot 4\text{H}_2\text{O}$ after dehydration and rehydration; Table S1: Enthalpy and entropy values for peaks observed in the DSC curve; Table S2: Intermolecular hydrogen bonds in the crystal structure of $1\cdot 4\text{H}_2\text{O}$; CIF data.

Author Contributions: V.J.-M. and F.M.R. jointly designed the experiments, made the synthesis and characterization of the compounds, analysed their thermal, structural, and magnetic properties, and wrote the manuscript. C.G.-S. collected the X-ray data and solved the crystal structure.

Acknowledgments: We wish to thank José M. Martínez-Agudo and Gloria Agustí for the magnetic measurements. We acknowledge financial support from the Spanish Ministerio de Ciencia, Innovación y Universidades (MICINN project CTQ2017-87201-P). V.J.-M. also extends thanks to the MICINN for an FPU fellowship (FPU15/02804).

Conflicts of Interest: The authors declare no conflict of interest.

References

1. Bartual-Murgui, C.; Akou, A.; Thibault, C.; Molnár, G.; Vieu, C.; Salmon, L.; Bousseksou, A. Spin-crossover metal-organic frameworks: Promising materials for designing gas sensors. *J. Mater. Chem. C* **2015**, *3*, 1277–1285. [[CrossRef](#)]
2. Kahn, O. Spin-transition polymers: From molecular materials toward memory devices. *Science* **1998**, *279*, 44–48. [[CrossRef](#)]
3. Senthil Kumar, K.; Ruben, M. Emerging trends in spin crossover (SCO) based functional materials and devices. *Coord. Chem. Rev.* **2017**, *346*, 176–205. [[CrossRef](#)]
4. Baadji, N.; Sanvito, S. Giant resistance change across the phase transition in spin-crossover molecules. *Phys. Rev. Lett.* **2012**, *108*, 1–5. [[CrossRef](#)] [[PubMed](#)]
5. Kahn, O. Spin-crossover molecular materials. *Curr. Opin. Solid State Mater. Sci.* **1996**, *1*, 547–554. [[CrossRef](#)]
6. Kahn, O. *Molecular Magnetism*; Wiley-VCH: New York, NY, USA; pp. 10010–14906.
7. Matsumoto, T.; Newton, G.N.; Shiga, T.; Hayami, S.; Matsui, Y.; Okamoto, H.; Kumai, R.; Murakami, Y.; Oshio, H. Programmable spin-state switching in a mixed-valence spin-crossover iron grid. *Nature Comm.* **2014**, *5*, 1–8. [[CrossRef](#)] [[PubMed](#)]
8. Li, Z.Y.; Ohtsu, H.; Kojima, T.; Dai, J.W.; Yoshida, T.; Breedlove, B.K.; Zhang, W.X.; Iguchi, H.; Sato, O.; Kawano, M.; Yamashita, M. Direct observation of ordered high-spin-low-spin intermediate states of an iron(III) three-step spin-crossover complex. *Angew. Chem. Int. Ed.* **2016**, *55*, 5184–5189. [[CrossRef](#)] [[PubMed](#)]
9. Osorio, E.A.; Moth-Poulsen, K.; Van Der Zant, H.S.J.; Paaske, J.; Hedegård, P.; Flensberg, K.; Bendix, J.; Bjørnholm, T. Electrical manipulation of spin states in a single electrostatically gated transition-metal complex. *Nano Lett.* **2010**, *10*, 105–110. [[CrossRef](#)] [[PubMed](#)]
10. Baadji, N.; Piacenza, M.; Tugsuz, T.; Della Sala, F.; Maruccio, G.; Sanvito, S. Electrostatic spin crossover effect in polar magnetic molecules. *Nature Mater.* **2009**, *8*, 813–817. [[CrossRef](#)] [[PubMed](#)]
11. Pinkowicz, D.; Rams, M.; Misek, M.; Kamenev, K.V.; Tomkowiak, H.; Katrusiak, A.; Sieklucka, B. Enforcing multifunctionality: A pressure-induced spin-crossover photomagnet. *J. Am. Chem. Soc.* **2015**, *137*, 8795–8802. [[CrossRef](#)] [[PubMed](#)]
12. Gallois, B.; Real, J.A.; Hauw, C.; Zarembowitch, J. Structural changes associated with the spin transition in bis(isothiocyanato)bis(1,10-phenanthroline)iron: A single-crystal x-ray investigation. *Inorg. Chem.* **1990**, *29*, 1152–1158. [[CrossRef](#)]
13. Miyamachi, T.; Gruber, M.; Davesne, V.; Bowen, M.; Boukari, S.; Joly, L.; Scheurer, F.; Rogez, G.; Yamada, T.K.; Ohresser, P.; et al. Robust spin crossover and memristance across a single molecule. *Nature Commun.* **2012**, *3*, 936–938. [[CrossRef](#)] [[PubMed](#)]
14. Bousseksou, A.; Molnár, G.; Demont, P.; Menegotto, J. Observation of a thermal hysteresis loop in the dielectric constant of spin crossover complexes: Towards molecular memory devices. *J. Mater. Chem.* **2003**, *13*, 2069–2071. [[CrossRef](#)]
15. Bousseksou, A.; Molnár, G.; Salmon, L.; Nicolazzi, W. Molecular spin crossover phenomenon: Recent achievements and prospects. *Chem. Soc. Rev.* **2011**, *40*, 3313–3335. [[CrossRef](#)] [[PubMed](#)]
16. Aromí, G.; Aguilà, D.; Gamez, P.; Luis, F.; Roubeau, O. Design of magnetic coordination complexes for quantum computing. *Chem. Soc. Rev.* **2012**, *41*, 537–546. [[CrossRef](#)] [[PubMed](#)]
17. Khusniyarov, M.M. How to switch spin-crossover metal complexes at constant room temperature. *Chem. Eur. J.* **2016**, *22*, 15178–15191. [[CrossRef](#)] [[PubMed](#)]
18. Gütllich, P.; Gaspar, A.B.; Garcia, Y. Spin state switching in iron coordination compounds. *Beilstein J. Org. Chem.* **2013**, *9*, 342–391. [[CrossRef](#)] [[PubMed](#)]
19. Niel, V.; Thompson, A.L.; Muñoz, M.C.; Galet, A.; Goeta, A.E.; Real, J.A. Crystalline-state reaction with allosteric effect in spin-crossover, interpenetrated networks with magnetic and optical bistability. *Angew. Chem. Int. Ed.* **2003**, *42*, 3760–3763. [[CrossRef](#)] [[PubMed](#)]

20. Niel, V.; Thompson, A.L.; Goeta, A.E.; Enachescu, C.; Hauser, A.; Galet, A.; Muñoz, M.C.; Real, J.A. Thermal- and photoinduced spin-state switching in an unprecedented three-dimensional bimetallic coordination polymer. *Chem. Eur. J.* **2005**, *11*, 2047–2060. [[CrossRef](#)] [[PubMed](#)]
21. Piñeiro-López, L.; Valverde-Muñoz, F.J.; Serebyuk, M.; Muñoz, M.C.; Haukka, M.; Real, J.A. Guest induced strong cooperative one- and two-step spin transitions in highly porous iron(II) hofmann-type metal-organic frameworks. *Inorg. Chem.* **2017**, *56*, 7038–7047. [[CrossRef](#)] [[PubMed](#)]
22. Murphy, M.J.; Zenere, K.A.; Ragon, F.; Southon, P.D.; Kepert, C.J.; Neville, S.M. Guest programmable multistep spin crossover in a porous 2-D Hofmann-type material. *J. Am. Chem. Soc.* **2017**, *139*, 1330–1335. [[CrossRef](#)] [[PubMed](#)]
23. Scudder, M.L.; Craig, D.C.; Goodwin, H.A. Hydrogen bonding influences on the properties of heavily hydrated chloride salts of iron(II) and ruthenium(II) complexes of 2,6-bis(pyrazol-3-yl)pyridine, 2,6-bis(1,2,4-triazol-3-yl)pyridine and 2,2':6',2''-terpyridine. *Cryst. Eng. Comm.* **2005**, *7*, 642–649. [[CrossRef](#)]
24. Sugiyarto, K.H.; Scudder, M.L.; Craig, D.C.; Goodwin, H.A. Electronic and structural properties of the spin crossover systems bis(2,6-bis(pyrazol-3-yl)pyridine)iron(II)thiocyanate and selenocyanate. *Aust. J. Chem.* **2000**, *53*, 755–765. [[CrossRef](#)]
25. Lochenie, C.; Bauer, W.; Railliet, A.P.; Schlamp, S.; Garcia, Y.; Weber, B. Large thermal hysteresis for iron(II) spin crossover complexes with *N*-(Pyrid-4-yl)isonicotinamide. *Inorg. Chem.* **2014**, *53*, 11563–11572. [[CrossRef](#)] [[PubMed](#)]
26. Weber, B.; Bauer, W.; Obel, J. An iron(II) spin-crossover complex with a 70 K wide thermal hysteresis loop. *Angew. Chem. Int. Ed.* **2008**, *47*, 10098–10101. [[CrossRef](#)] [[PubMed](#)]
27. Craig, G.A.; Roubeau, O.; Aromí, G. Spin state switching in 2,6-bis(pyrazol-3-yl)pyridine (3-bpp) based Fe(II) complexes. *Coord. Chem. Rev.* **2014**, *269*, 13–31. [[CrossRef](#)]
28. Létard, J.F.; Guionneau, P.; Nguyen, O.; Costa, J.S.; Marcén, S.; Chastanet, G.; Marchivie, M.; Goux-Capes, L. A guideline to the design of molecular-based materials with long-lived photomagnetic lifetimes. *Chem. Eur. J.* **2005**, *11*, 4582–4589. [[CrossRef](#)] [[PubMed](#)]
29. Marcén, S.; Lecren, L.; Capes, L.; Goodwin, H.A.; Létard, J.F. Critical temperature of the LIESST effect in a series of hydrated and anhydrous complex salts [Fe(bpp)₂]₂X₂. *Chem. Phys. Lett.* **2002**, *358*, 87–95. [[CrossRef](#)]
30. Buchen, T.; Gütlich, P.; Sugiyarto, K.H.; Goodwin, H.A. High-spin → low-spin relaxation in [Fe(bpp)₂](CF₃SO₃)₂·H₂O after LIESST and thermal spin-state trapping - Dynamics of spin transition versus dynamics of phase transition. *Chem. Eur. J.* **1996**, *2*, 1134–1138. [[CrossRef](#)]
31. Clemente-León, M.; Coronado, E.; Giménez-López, M.C.; Romero, F.M.; Asthana, S.; Desplanches, C.; Létard, J.-F. Structural, thermal and photomagnetic properties of spin crossover [Fe(bpp)₂]²⁺ salts bearing [Cr(L)(ox)₂]⁻ anions. *Dalton Trans.* **2009**, *38*, 8087–8095. [[CrossRef](#)] [[PubMed](#)]
32. Jornet-Mollá, V.; Duan, Y.; Giménez-Saiz, C.; Tang, Y.Y.; Li, P.F.; Romero, F.M.; Xiong, R.G. A ferroelectric iron(II) spin crossover material. *Angew. Chem. Int. Ed.* **2017**, *56*, 14052–14056. [[CrossRef](#)] [[PubMed](#)]
33. Lin, Y.; Lang, S.A. Novel two step synthesis of pyrazoles and isoxazoles from aryl methyl ketones. *J. Heterocycl. Chem.* **1977**, *14*, 345–347. [[CrossRef](#)]
34. Sheldrick, G.M. SHELX Version 2014/7. Available online: <http://shelx.uni-ac.gwdg.de/SHELX/index.php> (accessed on 20 November 2018).
35. Clemente-León, M.; Coronado, E.; Giménez-López, M.C.; Romero, F.M. Structural, thermal, and magnetic study of solvation processes in spin-crossover [Fe(bpp)₂][Cr(L)(Ox)₂]₂ nH₂O complexes. *Inorg. Chem.* **2007**, *46*, 11266–11276. [[CrossRef](#)] [[PubMed](#)]
36. Coronado, E.; Giménez-López, M.C.; Giménez-Saiz, C.; Romero, F.M. Spin crossover complexes as building units of hydrogen-bonded nanoporous structures. *Cryst. Eng. Comm.* **2009**, *11*, 2198–2203. [[CrossRef](#)]
37. Jornet-Mollá, V.; Duan, Y.; Giménez-Saiz, C.; Waerenborgh, J.C.; Romero, F.M. Hydrogen-bonded networks of [Fe(bpp)₂]²⁺ spin crossover complexes and dicarboxylate anions: Structural and photomagnetic properties. *Dalton Trans.* **2016**, *45*, 17918–17928. [[CrossRef](#)] [[PubMed](#)]
38. Sugiyarto, K.H.; McHale, W.A.; Craig, D.C.; Rae, A.D.; Scudder, M.L.; Goodwin, H.A. Spin transition centres linked by the nitroprusside ion. the cooperative transition in bis(2,6-bis(pyrazol-3-yl)-pyridine)iron(II) nitroprusside. *Dalton Trans.* **2003**, *12*, 2443–2448. [[CrossRef](#)]
39. Sugiyarto, K.H.; Goodwin, H.A. Coordination of Pyridine-Substituted Pyrazoles and Their Influence on the Spin State of Iron(II). *Aust. J. Chem.* **1988**, *41*, 1645–1663. [[CrossRef](#)]

40. Létard, J.F. Photomagnetism of iron(ii) spin crossover complexes—The T(LIESST) approach. *J. Mater. Chem.* **2006**, *16*, 2550–2559. [[CrossRef](#)]
41. Jaffé, H.H.; Doak, G.O. The basicities of substituted pyridines and their 1-oxides. *J. Am. Chem. Soc.* **1955**, *77*, 4441–4444. [[CrossRef](#)]



© 2018 by the authors. Licensee MDPI, Basel, Switzerland. This article is an open access article distributed under the terms and conditions of the Creative Commons Attribution (CC BY) license (<http://creativecommons.org/licenses/by/4.0/>).